



Unblocked intramolecular charge transfer for enhanced CO₂ photoreduction enabled by an imidazolium-based ionic conjugated microporous polymer

Wenling Zhao^a, Dong Zhai^a, Chengcheng Liu^{a,*}, Daoyuan Zheng^a, Hao Wu^a, Lei Sun^a, Zhen Li^a, Tie Yu^a, Wei Zhou^a, Xu Fang^a, Shengliang Zhai^a, Keli Han^{a,b}, Zuoli He^c, Wei-qiao Deng^{a,b}

^a Institute of Molecular Science and Engineering, Institute of Frontier and Interdisciplinary Science, Shandong University, Qingdao, Shandong 266237, PR China

^b State Key Laboratory of Molecular Reaction Dynamics, Dalian Institute of Chemical Physics, Chinese Academy of Sciences, Dalian 116023, PR China

^c Shandong Key Laboratory of Water Pollution Control and Resource Reuse, School of Environmental Science and Engineering, Shandong University, Qingdao, Shandong 266237, PR China

ARTICLE INFO

Keywords:

Carbon dioxide fixation
Conjugated microporous polymer
Intramolecular electron transfer
Imidazole
Photocatalysis

ABSTRACT

Efficient solar energy-driven conversion of CO₂ to valuable chemicals is challenging. Here we design an imidazolium-based ionic conjugated microporous polymer (ImI-CMP), which unblocks readily intramolecular charge transfer and triggers CO₂ photoreduction. Under visible light irradiation, ImI-CMP incorporated with Co (II) species exhibits a high CO production rate of 2953 μmol g⁻¹ h⁻¹ and a turnover frequency of 30.8 h⁻¹; these numbers are competitive to that of the best porous organic polymers. The mechanism studies reveal that two factors play key roles in the outstanding photocatalytic performance. First, the imidazolium motifs on the ImI-CMP enhance the activation of CO₂. Second, π-conjugation structure and the built-in electric field allow ultrafast intramolecular photoinduced electron transfer in the ImI-CMP. This work provides a new strategy for designing high-performance organic photocatalysts for CO₂ reduction by combining cationic imidazolium motifs and π-conjugation structures.

1. Introduction

Photoreduction of carbon dioxide (CO₂) represents a key technology for greenhouse gases emission-reduction and a truly balanced global carbon cycle, in which gaseous CO₂ is reduced into various chemical feedstocks [1,2]. However, activation of the inert CO₂ has proven to be very difficult due to its linear structure and the short C—O bond distance (1.16 Å) [3–5]. Developing high-efficient photocatalysts is one of the most pressing problems [5]. For heterogeneous photocatalysis, inorganic semiconductors (e.g. GaN, TiO₂) and organic semiconductors (e.g. covalent organic frameworks (COFs) and conjugated microporous polymers (CMPs)) are the two main families of photocatalysts [6–9]. In particular, organic semiconductor photocatalysts show distinct advantages over inorganic semiconductors in CO₂ adsorption and tunable optoelectronic properties [5,10,11]. Whereas, the main factors in hindering high photocatalytic efficiency are spontaneous charge-hole recombination and low electron transfer efficiency within the catalysts

[5,12–14]. CMPs are promising heterogeneous photocatalysts due to their intrinsic properties such as high chemical stability, adjustable band gaps, facile processing, high specific surface area and abundant pore structures [13,15–17]. In particular, the exploration of synthetic strategies for the construction of CMPs with electron donor (D) and acceptor (A) components is crucial for efficient photoinduced electron transfer. In principle, D-A systems can significantly promote the migration of electrons and holes in opposite directions (i.e., charge separation), which thus improves photocatalytic activity [16]. Nevertheless, the category of D-A motifs in the context of polymer photocatalysts still remains to be explored [18].

Imidazolium ionic liquids (ILs), imidazolyliene N-heterocyclic carbenes (NHCs), and zeolitic imidazolium frameworks with imidazolium motifs have been extensively explored for CO₂ adsorption and thermal catalytic conversion [2,19,20]. It has been proposed that ILs with imidazolium motifs can promote CO₂ capture and conversion [2,20]. The enhanced CO₂ conversion activities are attributed to the favorable

* Corresponding author.

E-mail address: chengcheng.liu@sdu.edu.cn (C. Liu).

<https://doi.org/10.1016/j.apcatb.2021.120719>

Received 23 July 2021; Received in revised form 6 September 2021; Accepted 10 September 2021

Available online 20 September 2021

0926-3373/© 2021 Elsevier B.V. All rights reserved.

imidazole- CO_2 interactions [21]. For example, Masel and coworkers reported that the imidazolium motif in ILs could lower the potential for formation of the $\text{CO}_2^{\bullet-}$ intermediate, which then reacts with H^+ on the cathode to produce CO in electroreduction of CO_2 [3,4]. To date, ILs have rarely been used in photocatalysis, if ever, the catalytic efficiency remains very low [20,21]. Additionally, it is impractical to extract liquid-phase products when using ILs as homogeneous catalysts or solvents, which thus incapacitates their reusability [4]. We were therefore inspired to integrate the unique coordination chemistry of imidazolium motifs with CMPs for photocatalytic CO_2 reduction. The incorporation of imidazolium cationic motifs as organic radical cations into organic frameworks brings ionic interfaces, which are expected to induce novel functions that are distinct from those with neutral skeletons [22–25].

Herein, we design an imidazolium-based ionic CMP (ImI-CMP), which enables the creation of a spatially confined ionic interface [22]. With the incorporation of Co(II) species, the ImI-CMP@Co nanocatalyst leapfrogs the photocatalytic CO_2 reduction reaction with an extraordinary activity (a CO production rate of $2953 \mu\text{mol g}^{-1} \text{h}^{-1}$ and a TOF of 30.8 h^{-1}) and durability. Interestingly, H_2 is another main product in this system, the accomplished $n(\text{H}_2)/n(\text{CO})$ stays around 2 along the whole reaction process, which is exactly the most desirable syngas for methanol synthesis [26]. The merits offered by this design strategy include: 1) The ionic pore walls with imidazolium motifs offer a microenvironment for CO_2 enrichment and activation [27]. 2) The π -conjugation structure and the built-in electric field could facilitate oriented intramolecular electron transfer [27,28]. This work proposes a new strategy for designing efficient photocatalysts by introducing a cationic motif as an electron acceptor and illuminate the roles of imidazolium motifs in CO_2 photoreduction.

2. Experimental section

2.1. Chemicals

All reagents were supplied by commercial company. Tetrakis-(triphenylphosphine) palladium(0), CuI were purchased from Sigma-Aldrich. 1,3-bis(4-bromophenyl)-1H-imidazol-3-ium bromide was purchased from Jilin Chinese Academy of Sciences – Yanshen Technology Co., Ltd. Nafion solution (5 wt%), tris(2,2'-bipyridine)ruthenium dichloride were purchased from Macklin Chemical Reagent Co., Ltd. Tetrakis(4-ethynylphenyl) methane was purchased from Shanghai Kylpharm Co., Ltd. Cobalt acetate tetrahydrate ($\text{Co}(\text{OAc})_2 \cdot 4\text{H}_2\text{O}$), triethanolamine (TEOA), acetonitrile (CH_3CN), N,N-dimethylformamide (DMF), acetone, tetrahydrofuran, sodium bromide were purchased from Sinopharm Chemical Reagent Co., Ltd. All above reagents were used without further purification.

2.2. Characterization

The FT-IR spectra were recorded by Bruker's VERTEX 70v in the range of $400\text{--}4000 \text{ cm}^{-1}$. The PXRD patterns were recorded with Cu-K α X-ray radiation source incident radiation by a Rigaku D-Max 2500 instrument, from $2\theta = 2^\circ$ up to 45° at a rate of $2^\circ/\text{min}$. The concentration of Co was analyzed by inductively coupled plasma optical emission spectrometry (ICP-OES; iCAP 7000, Thermo Fisher Scientific Inc.). Scanning electron microscopy (SEM) and energy dispersive X-ray absorption spectroscopy (EDS) analyses were carried out using a Quanta 250 FEG scanning electron microscope. Solid-state ^{13}C CP/MAS NMR was performed on an Bruker ADVANCE III HD 400 MHz spectrometer. High-resolution transmission electron microscopy was obtained with a JEOLJEM-2010F microscope. Thermogravimetric analysis was performed by using Netzsch Model STA449C instrument over the temperature range from room temperature to 800°C under Ar atmosphere. Gaseous products were detected using gas chromatography (Agilent Technologies-7890B). UV-vis spectra were recorded using an Agilent Cary 5000 spectrometer from 200 to 1400 nm. The PL spectra and time-

resolved PL decay spectra were measured by an FSL 1000 Edinburgh Instruments spectrofluorimeter at 25°C . Nanosecond transient absorption experiments (NTAS) were carried out on the CH_3CN solution using an LFP 1000 spectrometer at room temperature. Nitrogen sorption isotherms were measured at 77 K with Quantachrome Automated Surface Area & Pore Size Analyzer. Non-local density functional theory (NL-DFT) is used to estimate the pore size distribution. Before measurement, the samples were degassed in vacuum at 120°C for about 8 h.

2.3. Preparation of catalyst

2.3.1. Synthesis of ImI-CMP

A mixture of tetrakis(4-ethynylphenyl)methane (197.4 mg, 0.72 mmol), 1,3-bis(4-bromophenyl)-1H-imidazol-3-ium bromide (440 mg, 0.96 mmol), tetrakis-(triphenylphosphine)palladium (0) (66.6 mg, 0.06 mmol), and CuI (21.6 mg, 0.11 mmol) were degassed in a 100 mL flask and refilled with high purity nitrogen for 30 min. After that, a mixture solution of 20 mL DMF and 20 mL TEA was successively injected into the flask. The mixture solution was stirred at 100°C for 72 h under a nitrogen atmosphere. After cooling to room temperature, the precipitate was centrifuged and washed three times with DMF, THF, methanol, and acetone to remove unreacted monomer or residual catalysts, respectively. Thereafter, the brown solid was soaked in saturated aqueous sodium bromide solution for 24 h at room temperature to eliminate the possibility of counteranion exchange during the polymerization reaction. Then, the solid was filtered and washed with H_2O and methanol. The brown powder was further purified by Soxhlet extraction from methanol and THF for 48 h. The obtained products were dried under vacuum at 60°C for 12 h (yield: 494 mg, 73.4%).

2.3.2. Synthesis of ImI-CMP@Co

ImI-CMP@Co was synthesized by direct metallation of ImI-CMP with $\text{Co}(\text{OAc})_2 \cdot 4\text{H}_2\text{O}$ in a hydrothermal reaction. ImI-CMP (200 mg) and $\text{Co}(\text{OAc})_2 \cdot 4\text{H}_2\text{O}$ (400 mg) were degassed in a 100 mL flask for 30 min and refilled with high purity nitrogen. After that, 60 mL MeOH was successively injected into the flask. The mixture solution was stirred at 85°C for 72 h under a nitrogen atmosphere. After cooling to room temperature, the precipitate was centrifuged and washed with methanol to remove unreacted $\text{Co}(\text{OAc})_2 \cdot 4\text{H}_2\text{O}$. Thereafter, the obtained products were dried under vacuum at 60°C for 12 h to obtain the ImI-CMP@Co.

2.4. CO_2 Temperature-programmed desorption measurement

Temperature-programmed desorption (TPD) of carbon dioxide was carried out in a conventional apparatus by a Chemisorption Analyzer equipped with a TCD detector. Approximately 100 mg of catalyst was pretreated at 150°C for 1 h under an ultrahigh-purity Ar gas flow at a rate of 30 mL min^{-1} . Highly pure carbon dioxide was introduced at a constant temperature of 30°C under a flow rate of 30 mL min^{-1} for 60 min. Physically-adsorbed CO_2 was removed by exposure to ultrahigh-purity Ar at 30°C for 60 min. Then the temperature was increased to 310°C with a heating rate of $10^\circ\text{C min}^{-1}$ under ultrahigh-purity Ar. Finally, the desorbed CO_2 was monitored by a Chemisorption Analyser (Tp 5080 Chemisorb).

2.5. Photocatalytic reduction of CO_2

CO_2 reduction was conducted on a Labsolar-6A system (Beijing Perfectlight Technology Co., Ltd.). A mixed solution of MeCN and TEOA (4:1, 100 mL) containing ImI-CMP@Co (10 mg) and $[\text{Ru}(\text{bpy})_3]\text{Cl}_2$ (30 mg) was put in the container. After the gas in the container was removed via vacuum, CO_2 was injected to 80 kPa. Then, the mixture was irradiated by a 300 W Xe lamp ($\lambda > 420 \text{ nm}$) and stirred during photocatalytic reaction. An Agilent 8890 gas chromatograph was used to quantify the amount of CO. For the recirculation test, we used 50 mg catalyst and everything else remained the same. In the recovery experiment, the

catalyst was separated and washed with MeCN and then redispersed into a new mixture, and then a photocatalytic test was carried out under the same conditions as before. The TOF was calculated based on the ratio of CO production to metal content and time, i.e., $\text{TOF} = n_{\text{CO}} (\text{mol})/n_{\text{Co}} (\text{mol})/t (\text{h})$.

2.6. Photocurrent measurements

Two milligrams of ImI-CMP powder were mixed with 1.0 mL ethanol and 10 μL Nafion solutions and sonicated for 20 min. The resulting mixture was deposited evenly on the bottom $1 \times 2 \text{ cm}^2$ area of the ITO glass plates and left in air to dry. The electrochemical measurement was performed in MeCN solution containing 0.10 M tetrabutylammonium hexafluorophosphate (TBAPF₆) as an electrolyte at 298 K under CO₂ with the use of a carbon electrode as a counter electrode and a Hg/HgO electrode as a reference electrode. Photocurrent test is conducted at a constant voltage of 1.4 V vs. reversible hydrogen electrode (RHE).

2.7. Mott–Schottky plots

Two milligrams of CMP powder was mixed with 1.0 mL ethanol and 10 μL Nafion solutions and sonicated for 20 min. The resulting mixture was deposited evenly on a glassy carbon electrode and left in air to dry. Mott-Schottky measurements were performed on an electrochemical

workstation in 0.2 M Na₂SO₄ electrolyte with a Ag/AgCl electrode as the reference electrode and a Pt plate as the counter electrode.

2.8. Solid-state photoluminescence

PL spectra were recorded by a FSL 1000 Edinburgh Instruments spectrofluorimeter at 25 °C. The spectral acquisition was collected with excitation of 365 nm, and emission range from 380 nm to 900 nm. Decay time was calculated using 2 exponentials. All samples were tests on a quartz chip.

2.9. Nanosecond transient absorption spectroscopic

The measurements were carried out at ambient conditions using an LFP 1000 spectrometer. The solid sample was dispersed in acetonitrile. The spectral acquisition was collected with excitation of 355 nm, and emission range from 250 nm to 750 nm with 650 V voltage.

3. Results and discussion

3.1. Structural design of CMPs for CO₂ photoreduction

As the incorporation of imidazolium cationic motifs into organic frameworks are expected to make a breakthrough in CO₂

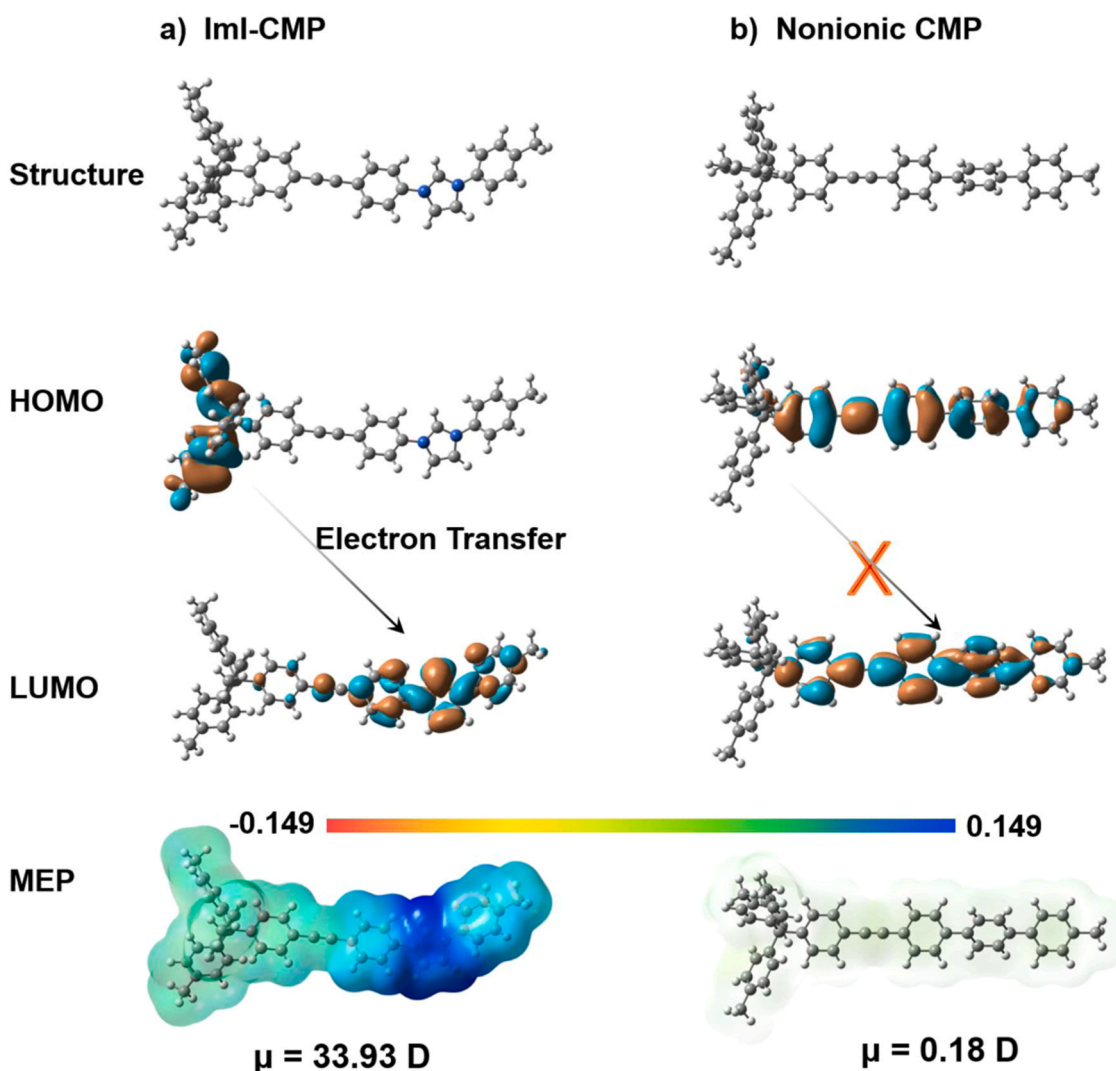


Fig. 1. Theoretical study. Frontier molecular orbitals (MOs) and molecular electrostatic potentials (MEPs) of ImI-CMP (a) and nonionic CMP (b).

photoreduction as distinct from those with neutral skeletons [22–25], we design a CMP with positively charged skeletons, i.e., ImI-CMP, and a CMP with neutral skeletons, i.e., nonionic CMP (Fig. 1). To forecast the effect of imidazolium cationic motifs on the localization of free- π -electrons, density functional theory (DFT) calculations at the

B3LYP-D3/6-31G(d,p) level of the theoretical study are carried out. The results show a substantial difference in the frontier orbital wave function for the ImI-CMP and nonionic CMP (Fig. 1a) [5,23]. For the ImI-CMP, the highest occupied molecular orbital (HOMO) is localized on the TEPM moiety and the lowest unoccupied molecular orbital (LUMO) is

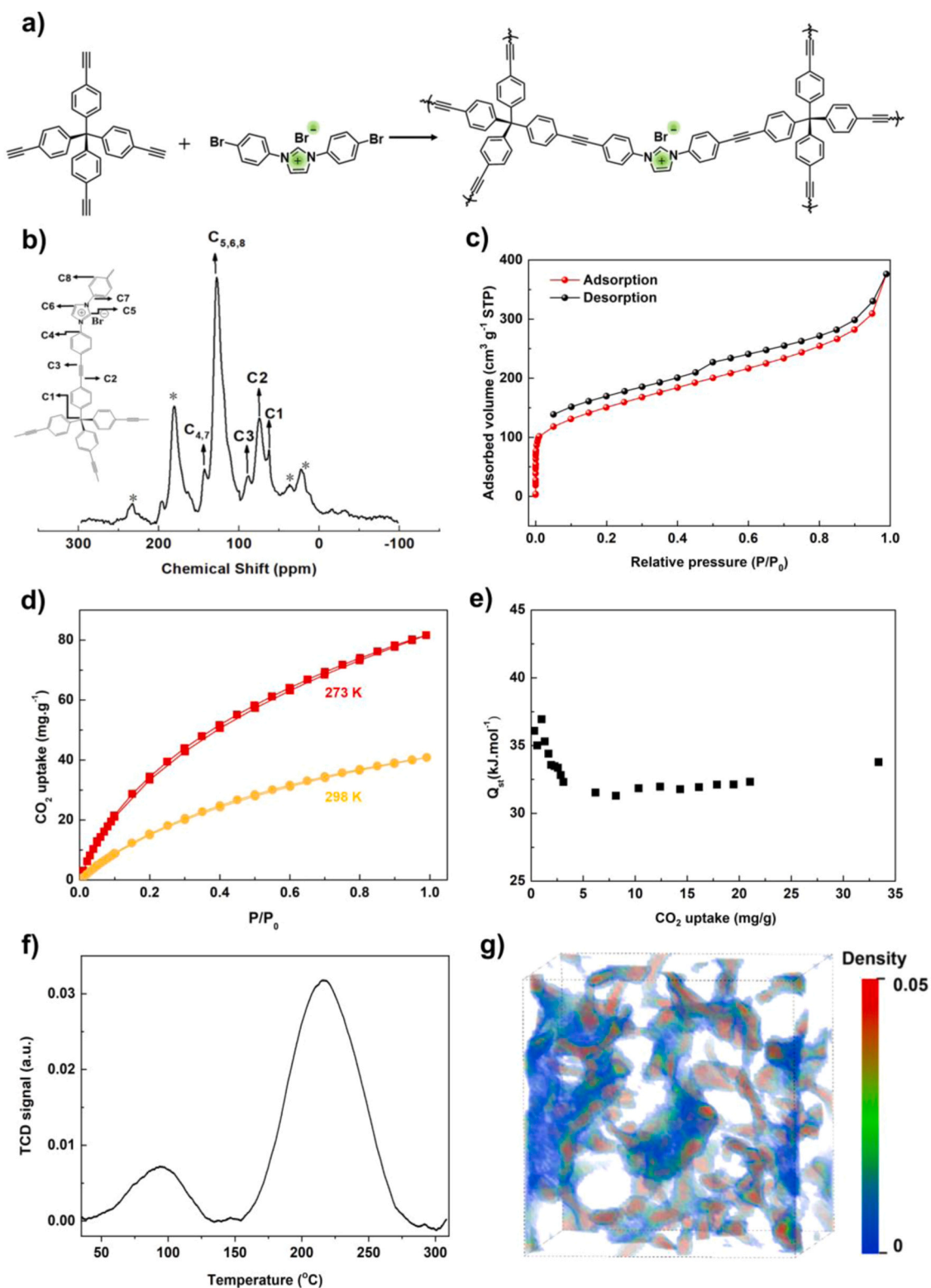


Fig. 2. Preparation and characterization of the ImI-CMP. (a) Scheme: synthetic strategy for the ImI-CMP. (b) ^{13}C solid-state NMR spectrum for the ImI-CMP. (c) N_2 adsorption/desorption isotherms for ImI-CMP. (d) CO_2 adsorption isotherms for ImI-CMP at 273 K and 298 K. (e) Q_{st} for CO_2 adsorption of the ImI-CMP. (f) CO_2 -TPD curve of the ImI-CMP. (g) Density field for CO_2 in the ImI-CMP computed by a Monte Carlo simulation at 273 K and a CO_2 pressure of 1 atm.

localized on the imidazolium moiety with an energy gap of 2.40 eV (Fig. 1a and Table S1). The ImI-CMP has a much larger molecular dipole (33.93 Debye) than the nonionic CMP (0.18 Debye), which can create a significant potential difference between the Tetrakis(4-ethynylphenyl) methane (TEPM) segments and the 1,3-bis(4-bromophenyl)-1H-imidazol-3-iumbromide (BPIB) segments (Fig. 1a) [29]. Moreover, the orientation of the dipole of the ImI-CMP is absolutely from the TEPM segment to the BPIB segment along the alkynyl (Fig. S1). Hence the presence of the imidazolium moiety generating a substantial difference in electrostatic potential offers a built-in electric field in ImI-CMP [29, 30]. Thus we give the hypothesis that the presence of cationic imidazolium moieties combined with the π -conjugation structure of ImI-CMP has an intramolecular electron transfer (CT) character from the TEPM segment to the BPIB segment upon light irradiation [23]. For the nonionic CMP, the distributions of HOMO and LUMO remain almost the same (Fig. 1b), and the segments do not have an electrostatic potential difference. This intramolecular charge transfer in ImI-CMP is expected to induce faster photogenerated carrier separation efficiency and promoted photocatalytic CO₂ reduction property.

3.2. Synthesis and structural characterization of ImI-CMP

To verify this design concept, the corresponding experiments are carried out based on the simulated results above. This ImI-CMP is first synthesized through the combination of ionic linkers and neutral knots via Sonogashira-Hagihara cross-coupling reaction (Fig. 2a). TEPM is used as a neutral knot and BPIB as cationic linker for the construction of the ImI-CMP in which the cationic sites are exposed to the wall surface. This polymer network is designed to have a three-dimensional net structure arising from the four-pronged arylene-ethynylene linkages. The structure of the ImI-CMP is characterized by Fourier transform infrared spectroscopy (FT-IR), solid-state cross polarization magic-angle spinning (CP-MAS) ¹³C NMR, N₂ adsorption/desorption isotherms, powder X-ray diffraction (PXRD) and elemental analysis. The chemical structures of the obtained ImI-CMP are confirmed by FT-IR (Fig. S2). The peak at 2209 cm⁻¹ of the ImI-CMP indicates the formation of $\text{—C}\equiv\text{C—}$ bonds [31]. The peak at 3284 cm⁻¹ assigned to $\text{—C}\equiv\text{C—H}$ in the TEPM disappears after the cross-coupling reaction, proving the total conversion of the precursor. ImI-CMP is extensively characterized using ¹³C solid-state NMR (Fig. 2b). The peak located at 63.0 ppm is attributed to the quaternary carbon core of tetraphenyl methane. The peaks at 128.5 ppm and 143.2 ppm correspond to aromatic C-C and C-H sites, while the peaks at 75.4 ppm and 88.5 ppm belong to C(sp)-C(sp) and C(sp)-C(sp²) sites [32]. These also verify the successful synthesis of the ImI-CMP [15].

The ImI-CMP exhibits a reversible type I isotherm in combination with type IV characteristics in N₂ adsorption-desorption analysis (Fig. 2c). The rapid increase at a relatively low-pressure range (below $P/P_0 = 0.01$) indicates the permanent microporous nature of the ImI-CMP. The hysteresis loop in a higher relative pressure range could be attributed to the presence of mesopores. The pore-size distribution curve is shown in Fig. S3. Micropores and mesopores centered at 0.57 nm, 1.42 nm and 3.39 nm give a total pore volume of 0.583 cm³ g⁻¹, in which the micropore volume is 0.078 cm³ g⁻¹. It is calculated that the Brunauer-Emmett-Teller (BET) surface area of the ImI-CMP is 529 m² g⁻¹, in which the micropore surface area is 166 m² g⁻¹. The PXRD pattern shows that the obtained ImI-CMP is amorphous, without any crystalline phase or catalyst residues (Fig. S4). As cationic polymers face problems with chemical stability, we also investigate the thermal stability of the ImI-CMP by thermogravimetric testing (TG) [15]. The ImI-CMP exhibits exceptional thermal stability and remains stable up to 320 °C under an Ar atmosphere presumably due to the well-spaced charged groups within the three-dimensional network (Fig. S5). The slight weight loss below 200 °C mostly results from the trapped solvent molecules in the pores. High-resolution transmission electron microscopy (HRTEM) and scanning electron microscopy (SEM) analyses are

used to investigate the bulk-scale morphology of ImI-CMP (Fig. S6). As we can see from the HRTEM images, the ImI-CMP is highly microporous. SEM images indicate that the ImI-CMP forms 3D mesoporous networks composed of spherical particles with a size distribution centered at 20 nm. The distribution of the C/N/Br in the ImI-CMP are verified by elemental mapping under SEM mode (Fig. S7). Element analytical tests suggest that the contents of C, N, H and Br are 63.5%, 6.0%, 4.5% and 8.0%, respectively. In addition, the nonionic CMP is also synthesized as comparison (Figs. S8 and S9).

3.3. CO₂ adsorption properties of the ImI-CMP

It was reported that the introduction of ionic surfaces in COFs can enhance the CO₂ affinity through dipole-quadrupole interactions and the CO₂ adsorption isotherms of the ImI-CMP are measured up to 1 bar at 273 K and 298 K [22]. The CO₂ adsorption isotherms display reversible adsorption capacity (Fig. 2d). When the actual pressure P of CO₂ approaches 760 mm Hg ($P/P_0 = 1$), the CO₂ uptake reach 82 mg g⁻¹ and 41 mg g⁻¹ at 273 K and 298 K, respectively [33,34]. All of the trapped CO₂ can be totally released at $P/P_0 = 0$. The adsorption isosteric heat Q_{st} calculated from the temperature-dependent CO₂ adsorption isotherms (273 K and 298 K) is in a narrow range (31–37 kJ mol⁻¹) and decrease initially from ~ 37 kJ mol⁻¹ to ~ 32 kJ mol⁻¹ for CO₂ uptakes of 0.3–6 mg g⁻¹. It then remains steady for CO₂ uptakes up to 34 mg g⁻¹ (Fig. 2e) [34]. The Q_{st} is much higher than most of the reported COFs, CMPs and MOFs, e.g., ~ 22 kJ mol⁻¹ for TpBpy-COF, ~ 22 kJ mol⁻¹ for Por-sp²c-COF, ~ 25 kJ mol⁻¹ for PCP-Cl and ~ 27 kJ mol⁻¹ for MFM-300 (In)-t. [15,35–37]. The high Q_{st} can be evidence of the strong electrostatic interactions between CO₂ molecules and the charged skeletons along with the ionic surface within the pores [15].

To evaluate CO₂ chemisorption on the ImI-CMP, CO₂-temperature programmed desorption (CO₂-TPD) experiment is performed (Fig. 2f). The TPD curve shows two CO₂ desorption peaks at 50–130 °C and 160–280 °C. Apart from the weakly adsorbed CO₂ below 100 °C, desorption around 160–280 °C can be associated with CO₂ molecules that are strongly adsorbed on the ImI-CMP [38]. In contrast, the TPD curve of the nonionic CMP shows no CO₂ desorption at temperatures up to 320 °C (Fig. S10). These results indicate that the chemisorption of CO₂ in the ImI-CMPs mainly occurs on the imidazolium motifs. The simulation in MAPS was used to further study the CO₂ adsorption behavior visually in the ImI-CMP. The porous structure leaves enough space between cationic sites which enables the accessibility of the cationic sites by CO₂ molecules [22]. The microporosity of this ImI-CMP stems from the rigid but contorted backbone [39]. The distribution of CO₂ adsorbed on ImI-CMP obtained from the Monte Carlo simulation at 273 K and 1 bar is shown in Fig. 2g. The density field for CO₂ in the ImI-CMP shows that the CO₂ molecules occupied the pores in the ImI-CMP. The porous structure of the ImI-CMP can enrich the adsorption of CO₂ [40].

3.4. CO₂ photoreduction

Due to the high affinity of ImI-CMP to CO₂ and its excellent chemical stability, the photoreduction of CO₂ is conducted with ImI-CMP@Co as the catalyst in 0.8 bar of CO₂ under visible light ($\lambda > 420$ nm). Co (II) has been recognized as one of the most active centers for adsorbing and activating CO₂ molecules and even for achieving photocatalytic CO₂ reduction [28,41,42]. Here we synthesize the ImI-CMP@Co from the ImI-CMP and cobalt acetate. The XPS spectrum shows the presence of C, N, O, and Co in ImI-CMP@Co (Fig. S11a). The observed Co 2p_{3/2} binding energy of 781.5 eV with a shakeup satellite at 786.5 eV in ImI-CMP@Co is consistent with Co (II) indicating the successful loading of Co ions into ImI-CMP (Fig. S11b) [42]. The N 1s signal of ImI-CMP and ImI-CMP@Co can be deconvoluted into 3 peaks at 398.5, 399.6 and 401.2 eV, respectively (Fig. S11c and d). Particularly, the peak at 398.5 eV can relative to pyridinic-N in ImI-CMP and pyridinic-N/Co-N in

ImI-CMP@Co. The binding energy of 398.5 eV in ImI-CMP@Co is much stronger than that in ImI-CMP, signifying the existence of Co—N bonds to anchor the metallic Co^{2+} [43,44].

For the photocatalytic CO_2 reduction, $[\text{Ru}(\text{bpy})_3]\text{Cl}_2$ (bpy = 2,2'-bipyridine) was used as a visible-light photosensitizer, and triethanolamine (TEOA) was adopted as an electron donor. CO and H_2 are detected as the main products (Figs. 3a and b and S12). ImI-CMP@Co exhibits excellent activity with a CO production rate of $2953 \mu\text{mol g}^{-1} \text{h}^{-1}$ and a turnover frequency (TOF) of 30.8 h^{-1} in 35 min [11,42]. The apparent quantum efficiency (AQE) at 420 nm is calculated to be 0.52% (Xe lamp current = 15 A, light intensity = 34.6 mW cm^{-2} , 10 mg ImI-CMP@Co catalyst). The CO production rate and TOF for CO evolution in 3.5 h remain high at $1884 \mu\text{mol g}^{-1} \text{h}^{-1}$ and 19.5 h^{-1} , which far outstrip the ImI-CMP (Fig. 3a). The TOF and CO production rate are competitive to the state-of-art porous photocatalysts (Table S2). Other examples include a CO production rate of $1020 \mu\text{mol g}^{-1} \text{h}^{-1}$ (TOF = 0.55 h^{-1} in 4 h) for DQTP COF-Co [42], $1213.33 \mu\text{mol g}^{-1} \text{h}^{-1}$ in 1 h for CMP-BT [45], $2274 \mu\text{mol g}^{-1} \text{h}^{-1}$ (TOF = 3.71 h^{-1} in 5 h) for N-CP-D [28], $469 \mu\text{mol g}^{-1} \text{h}^{-1}$ in 4 h for CNU-BA [46]. To identify the function of the imidazolium motifs in the ImI-CMP in improving the photoreduction of CO_2 to CO, the CMP without imidazolium motifs (Fig. 3a) is also employed in the catalytic reaction. Under identical reaction conditions, the CO production rate was much lower with nonionic CMP@Co as the catalyst, indicating the key role of imidazolium motifs in the photocatalytic reaction [3,4,20,23].

The simultaneous production of CO and H_2 (syngas) with fixed CO/ H_2 ratios has been considered very useful, which can be subsequently utilized in achieving value-added feedstocks through following thermochemical processes, e.g., Fischer–Tropsch process and methanol synthesis reactions [47,48]. The conventional approaches to syngas are based on reforming non-renewable fossil fuels (e.g., coal, petroleum coke and natural gas) operating at high temperatures of 800–1000 °C and pressures of 5–40 bar [48–50]. While the CO/ H_2 ratio is very important for controlling the different downstream products selectivity, producing the desired CO/ H_2 ratio with CO_2 as a feedstock is still challenging [47]. Interestingly, the $n(\text{H}_2)/n(\text{CO})$ in this photocatalytic CO_2 reduction process by the ImI-CMP@Co keeps ~ 2 (Figs. 3b and S12), which is a proper proportion exclusively for methanol production [49–51].

A series of control experiments are performed to identify the key factors for CO_2 -to-CO conversion (Fig. 3b). When photocatalytic experiments are performed with N_2 instead of CO_2 under the same reaction conditions, CO was not detected (Fig. 3b), which preliminarily proves that CO originates from CO_2 . No CO is detected under the conditions without light irradiation or in the absence of photosensitizer and triethanolamine. These indicate the necessity for light, photosensitizer and triethanolamine in the CO_2 reduction process. To further confirm the origin of the CO, isotope-labeled carbon dioxide ($^{13}\text{CO}_2$) is employed as a substitute source gas on a GC-MS system [28]. ^{13}CO is observed in the gas chromatogram and mass spectrum (a peak at $m/z = 29$) (Fig. 3c).

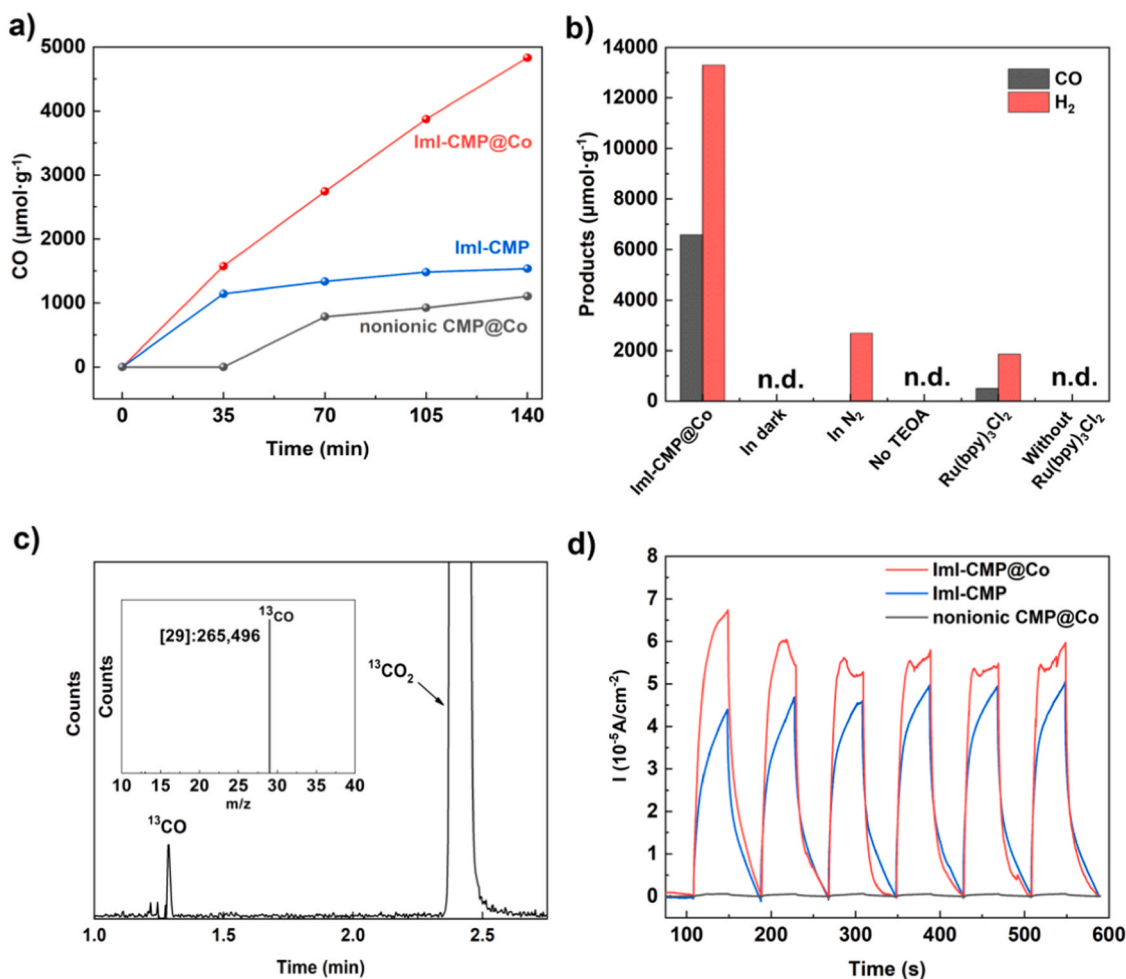


Fig. 3. Photocatalytic CO_2 reduction performance of the ImI-CMP, ImI-CMP@Co and nonionic CMP@Co. (a) Photocatalytic evolution of CO by ImI-CMP@Co, ImI-CMP and nonionic CMP@Co. (b) CO and H_2 production rate in 245 min under different conditions as comparative experiments. (c) Gas chromatogram and mass spectra ($m/z = 29$) analyses of the carbon source of the generated CO from the photocatalytic reduction of $^{13}\text{CO}_2$ using ImI-CMP@Co as catalysts. (d) Photocurrent measurement of ImI-CMP@Co, ImI-CMP and nonionic CMP@Co.

These results demonstrate that the carbon source of the formed CO was CO₂. In addition, the amount of photosensitizer, solvent proportion and the sacrificial agent type also affect the rate of CO₂ reduction to some extent (Figs. S13 and 14). The stability of ImI-CMP@Co is examined by running the experiments over 140 min for five cycles (Fig. S15). We also tested CO production over a longer period of time of 385 min, which shows constant photocatalytic activity (Fig. S16). The test demonstrates that the catalyst has good stability during the photocatalytic reactions. In addition, there is no obvious change in catalyst structures and morphology as observed in the SEM images of the ImI-CMP@Co before and after reaction (Fig. S17). In addition to SEM, we used FT-IR test before and after the catalytic reaction to characterize its chemical stability (Fig. S18). The FT-IR spectrum of the catalyst after reaction shows

the additional peak of the photosensitizer [Ru(bpy)₃]Cl₂ at 3166 cm⁻¹, indicating the adsorption of [Ru(bpy)₃]Cl₂ in the pores of the ImI-CMP@Co, which may result in poor CO₂ adsorption and slight decline of cyclic stability [52].

4. Mechanistic study

4.1. Spectroscopic characterization of the ImI-CMP and ImI-CMP@Co

To study the photoelectric properties of ImI-CMPs, photocurrent test is conducted (Fig. 3d). The ImI-CMPs photocathodes show high photocurrent (67 $\mu\text{A cm}^{-2}$ for ImI-CMP@Co and 43 $\mu\text{A cm}^{-2}$ for ImI-CMP photoanode). The extremely high photocurrent shows a greatly

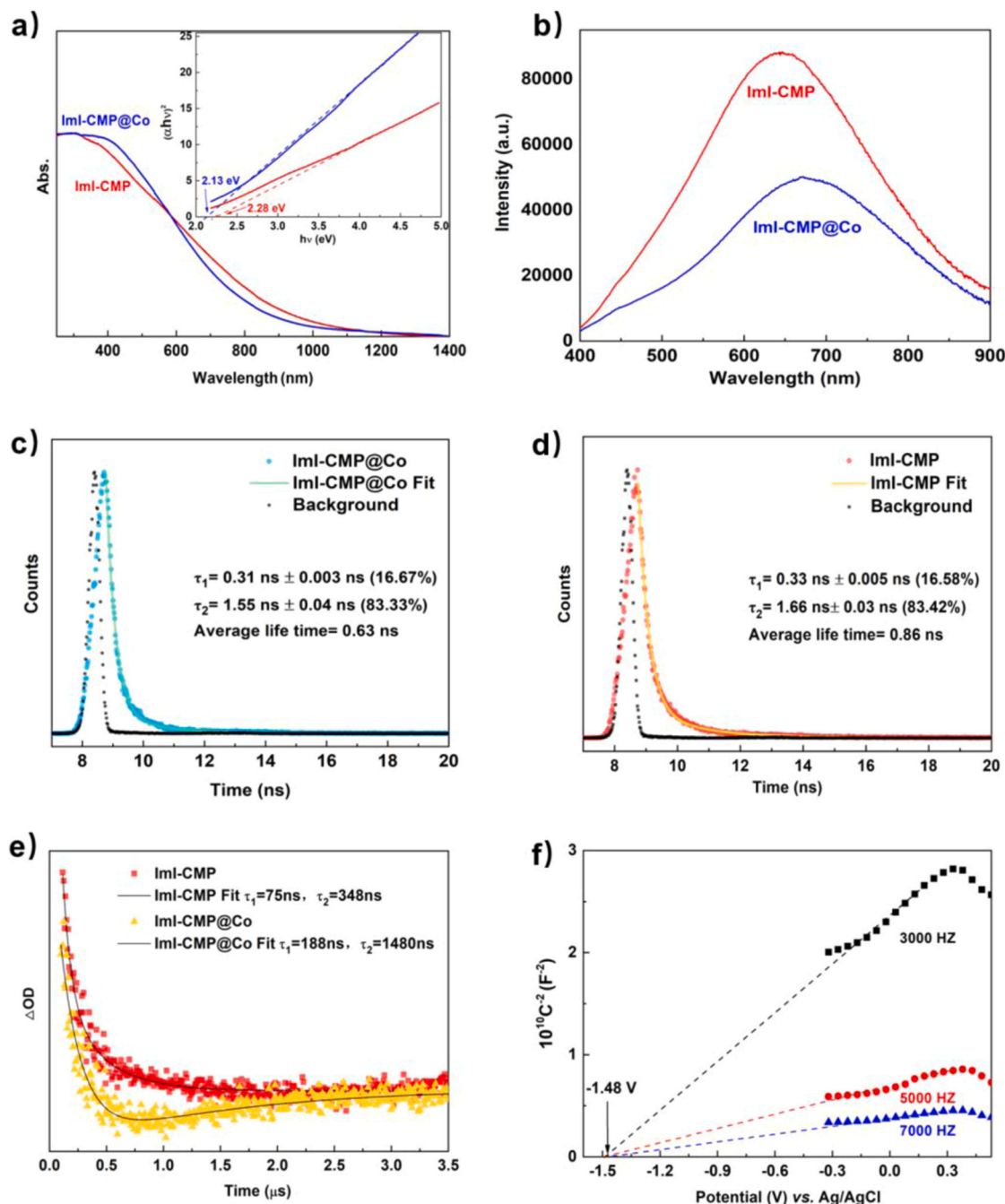


Fig. 4. Characterizations of catalysts. (a) Solid-state UV-vis spectra of the ImI-CMP and ImI-CMP@Co. (b) PL spectra of the ImI-CMP and ImI-CMP@Co. (c) Time-resolved PL decay spectra of the ImI-CMP. (d) Time-resolved PL decay spectra of the ImI-CMP@Co. (e) Nanosecond transient absorption spectra of the ImI-CMP and ImI-CMP@Co. (f) Mott-Schottky plots of the ImI-CMP@Co.

improved transient photocurrent when the ImI-CMPs photocathodes are illuminated with visible light. The much higher photocurrent of the ImI-CMPs photocathodes indicate high electrical conductivity and long lifetime of charge carriers in ImI-CMPs (Fig. 3d). These results show that ImI-CMP@Co acts as a better photoelectrocatalyst with faster charge separation and transfer. Moreover, the photocurrents of the nonionic CMP@Co are two orders of magnitude lower than ImI-CMP and ImI-CMP@Co, indicating that the presence of imidazolium motifs is crucial for fast charge separation and transfer.

To gain more mechanistic insights into the photocatalytic reduction of CO₂ by ImI-CMP@Co, we conduct spectroscopic characterization of the CMPs. The UV–vis absorption spectra of ImI-CMP and ImI-CMP@Co show good UV and visible light ($\lambda > 420$ nm) absorption performance (Fig. 4a) [42]. The intramolecular charge transfer behavior of ImI-CMP is investigated by solid-state photoluminescence (PL) and time-resolved fluorescence decay techniques. The PL of ImI-CMP@Co shows much weaker intensity than the ImI-CMP (Fig. 4b), illustrating that the existence of Co²⁺ can effectively prevent electron-hole recombination and quench the PL intensity. Thus the Co incorporation on ImI-CMP could enhance the electron transfer for the following photoreduction of CO₂. The average fluorescence life expectancies of the ImI-CMP and ImI-CMP@Co are 0.86 and 0.63 ns (Fig. 4c and d). The shorter life expectancies of the ImI-CMP@Co can be attributed to the fast delivery of photogenerated electrons from the ImI-CMP to cobalt ions [11]. Moreover, the PL decay spectra of the nonionic CMPs show much stronger PL intensity (Figs. S19 and S20), which suggests a weak ability of the nonionic CMP to suppress the recombination of excited state [42]. Nanosecond transient absorption (TA) spectroscopic studies are also carried out on the CMPs to further explore the photophysics of the system. The TA spectroscopy of the ImI-CMP and ImI-CMP@Co are conducted at 355 nm to reflect the degradation on the exciton and charge carrier dynamics in real time [53]. The spectrum of ImI-CMP is fitted with $\tau_1 = 75$ ns (52%) and $\tau_2 = 348$ ns (48%). ImI-CMP@Co is fitted with $\tau_1 = 188$ ns (41%) and $\tau_2 = 1480$ ns (59%), indicating the generation of a much longer lifetime of photogenerated carriers on the surface of ImI-CMP@Co (Fig. 4e). The significantly prolonged lifetime and the larger proportion of τ_2 demonstrate that the separation of electron-hole pairs is greatly promoted after the incorporation of Co [10,

52]. The efficient electron transfer is important for the photoreduction reactions [11,54]. All the above results reveal that ImI-CMP@Co is favorable for promoting photogenerated electron transfer during the photocatalytic CO₂ reduction process. This in turn endows ImI-CMP@Co with high photocatalytic CO₂ reduction activity [11].

The Mott-Schottky plots are measured at three frequencies (Figs. 4f and S21). The positive slopes of the curves indicate that the ImI-CMP is a typical n-type semiconductor [55]. The flat band potentials of ImI-CMP@Co is approximately -1.48 V vs Ag/AgCl (ImI-CMP@Co) at pH = 7. The following equation is used to convert the obtained potential (vs. Ag/AgCl) to NHE at pH = 7 [56].

$$E_{\text{NHE}} = E_{\text{AgCl}} + E_{\text{AgCl}}^0$$

$$E_{\text{AgCl}}^0 (3.5 \text{ M KCl}) = 0.2046 \text{ V at } 25^\circ\text{C}.$$

Hence ImI-CMP@Co have enough negative potential to enable the reduction of CO₂ to CO (-0.53 V vs NHE at pH = 7) [27]. By contrast, the flat band potentials of nonionic CMP and nonionic CMP@Co are -0.22 V and -0.36 V (Figs. S22 and S23), which are too low to reduce CO₂. These results are well consistent with the photocatalytic CO₂ reduction results.

Together, these spectroscopic and DFT results above point to a possible mechanistic pathway for the photocatalytic reduction of CO₂ over ImI-CMP@Co (Fig. 5). CO₂ is first concentrated around the imidazolium motif inside the pores. Upon light irradiation, [Ru(bpy)₃]²⁺ is converted to the excited state ^{*}[Ru(bpy)₃]²⁺. Then the photogenerated electrons are transferred to the ImI-CMP and the TEOA consumes the produced holes [35,42]. Meanwhile, intramolecular charge transfer occurs inside the ImI-CMP with the effect of built-in electric field. The electron-rich TEPM segment acts as an electron donor. The positively BPIB segment with imidazolium cations is electron-deficient and acts as an electron acceptor [23]. The photoexcited electrons on the TEPM segment then transfer to the BPIB segment in the built-in electric field with alkynyl as a bridge [28]. The electrons immediately transfer from the imidazolium motif on the BPIB segment to the Co site. The CO₂ obtain electrons from the Co site to form CO₂^{•-}. According to previous literature [3,4,20,23], the imidazolium motif in ImI-CMP can lower the potential for formation of the CO₂^{•-} intermediate. The ion pairing

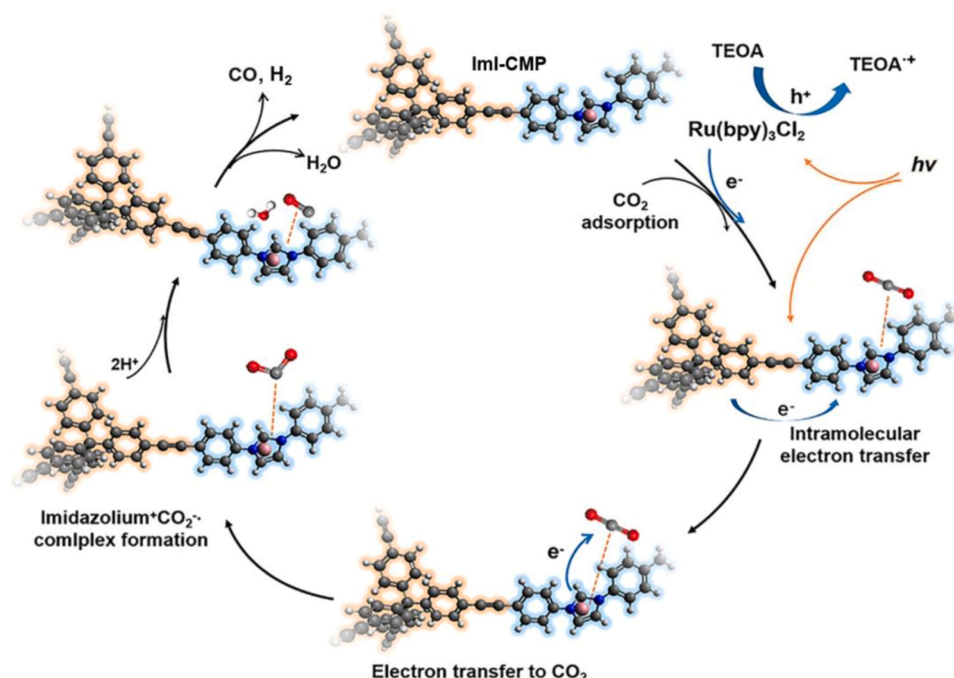


Fig. 5. Photocatalytic mechanism. Proposed catalytic mechanism of CO₂ reduction with ImI-CMP@Co.

between the imidazolium cation and $\text{CO}_2^{\bullet-}$ changes the active intermediate from the high-energy $\text{CO}_2^{\bullet-}$ ion radical to an imidazolium $^+\text{CO}_2^{\bullet-}$ complex [3,4,20,23]. The linear $\text{C}=\text{O}=\text{C}$ bond angle is bent when ion pairing occurs at the interface of the ImI-CMP [4]. This complex intermediate then undergo reduction to form CO, which is then released from the ImI-CMP surface, regenerating the uncomplexed imidazolium cation in the catalytic cycle. This cascaded electron pathway enables oriented electron delivery from the ImI-CMPs to metal sites and achieves an efficient system for CO_2 photoreduction [28].

5. Conclusions

In summary, we design and synthesize an imidazolium-based ionic CMP and demonstrate that this ImI-CMP could be an ideal platform for CO_2 photoreduction. The imidazolium motif on the ImI-CMP offers a microenvironment favorable for both CO_2 capture and CO_2 activation, which can reduce the potential for formation of the imidazolium $^+\text{CO}_2^{\bullet-}$ intermediate. The built-in electric field in the ImI-CMP provides a driving force for the separation and oriented transportation of photo-generated electrons. Meanwhile, the π -conjugation structure provided an intermolecular cascaded channel for the electrons transportation to achieve efficient CO_2 photoreduction. This strategy will open up new opportunities in tailoring the photocatalyst structure for fast photoinduced charge transfer.

CRedit authorship contribution statement

Wen-ling Zhao: Investigation, Methodology, Writing – original draft. **Dong Zhai:** Investigation, Software, Methodology. **Cheng-cheng Liu:** Conceptualization, Supervision, Writing – original draft. **Dao-yuan Zheng:** Methodology. **Hao Wu:** Investigation, Writing – review & editing. **Lei Sun:** Investigation, Software, Methodology. **Zhen Li:** Methodology. **Tie Yu:** Methodology. **Wei Zhou:** Methodology. **Xu Fang:** Methodology. **Sheng-liang Zhai:** Methodology. **Ke-li Han:** Investigation. **Zuo-li He:** Investigation. **Wei-qiao Deng:** Conceptualization, Supervision, Writing – review & editing.

Declaration of Competing Interest

The authors declare that they have no known competing financial interests or personal relationships that could have appeared to influence the work reported in this paper.

Acknowledgements

This work was supported by the National Key Research and Development Program of China (No. 2017YFA0204800), National Natural Science Foundation of China (No. 22003031), Natural Science Foundation of Shandong Province (No. ZR2020QB080) and Fundamental Research Funds of Shandong University (No. 2019GN109). C. C. L. thank the financial support from the Program of Young Scholars Future Program of Shandong University. H.W. thank the financial support from the Program of Qilu Young Scholars of Shandong University.

Appendix A. Supporting information

Supplementary data associated with this article can be found in the online version at doi:10.1016/j.apcatb.2021.120719.

References

- [1] E. Beckman, Sustainable chemistry putting carbon dioxide to work, *Nature* 531 (2016) 180–181.
- [2] M. Asadi, K. Kim, C. Liu, A.V. Ad Depalli, P. Abbasi, P. Yasaei, P. Phillips, A. Behranginia, J.M. Cerrato, R. Haasch, P. Zapol, B. Kumar, R.F. Klie, J. Abiad, L. A. Curtiss, Nanostructured transition metal dichalcogenide electrocatalysts for CO_2 reduction in ionic liquid, *Science* 353 (2016) 467–470.
- [3] B.A. Rosen, A. Salehi-Khojin, M.R. Thorson, Z. Wei, D.T. Whipple, P.J.A. Kenis, R. I. Masel, Ionic liquid-mediated selective conversion of CO_2 to CO at low overpotentials, *Science* 334 (2011) 643–644.
- [4] B.A. Rosen, I. Hod, Tunable molecular-scale materials for catalyzing the low-overpotential electrochemical conversion of CO_2 , *Adv. Mater.* 30 (2018), 1706238.
- [5] W. Huang, J. Byun, I. Rich, C. Ramanan, P.W.M. Blom, H. Lu, D. Wang, L. CairedaSilva, R. Li, L. Wang, K. Landfester, K.A.I. Zhang, Asymmetric covalent triazine framework for enhanced visible-light photoredox catalysis via energy transfer cascade, *Angew. Chem. Int. Ed. Engl.* 57 (2018) 8316–8320.
- [6] R. Li, W. Cheng, M.H. Richter, J.S. DuChene, W. Tian, C. Li, H.A. Atwater, Unassisted highly selective gas-phase CO_2 reduction with a plasmonic Au/p-GaN photocatalyst using H_2O as an electron donor, *ACS Energy Lett.* 6 (2011) 1849–1856.
- [7] Y. Xu, M. Yang, B. Chen, X. Wang, H. Chen, D. Kuang, C. Su, A CsPbBr₃ perovskite quantum dot/graphene oxide composite for photocatalytic CO_2 reduction, *J. Am. Chem. Soc.* 139 (2017) 5660–5663.
- [8] Z.-A. Lan, G. Zhang, X. Chen, Y. Zhang, K.A.I. Zhang, X. Wang, Reducing the exciton binding energy of donor–acceptor-based conjugated polymers to promote charge-induced reactions, *Angew. Chem. Int. Ed. Engl.* 58 (2019) 10236–10240.
- [9] C. Han, P. Dong, H. Tang, P. Zheng, C. Zhang, F. Wang, Realizing high hydrogen evolution activity under visible light using narrow band gap organic photocatalysts, *Chem. Sci.* 12 (2011) 1796–1802.
- [10] S. Yang, W. Hu, X. Zhang, P.L. He, B. Pattengale, C. Liu, M. Cendejas, I. Hermans, X. Zhang, J. Zhang, 2D covalent organic frameworks as intrinsic photocatalysts for visible light-driven CO_2 reduction, *J. Am. Chem. Soc.* 140 (2018) 14614–14618.
- [11] W. Liu, X. Li, C. Wang, H. Pan, W. Liu, K. Wang, Q. Zeng, R. Wang, J. Jiang, A scalable general synthetic approach toward ultrathin imine-linked two-dimensional covalent organic framework nanosheets for photocatalytic CO_2 reduction, *J. Am. Chem. Soc.* 141 (2019) 17431–17440.
- [12] T. Luo, J. Zhang, X. Tan, C. Liu, T. Wu, W. Li, X. Sang, B. Han, Z. Li, G. Mo, X. Xing, Z. Wu, Water-in-supercritical CO_2 microemulsion stabilized by a metal complex, *Angew. Chem. Int. Ed. Engl.* 55 (2016) 13533–13537.
- [13] Y.S. Kochergin, D. Schwarz, A. Acharjya, A. Ichangi, R. Kulkarni, P. Eliášová, J. Vacek, J. Schmidt, A. Thomas, M.J. Bojdy, Exploring the “Goldilocks Zone” of semiconducting polymer photocatalysts by donor–acceptor interactions, *Angew. Chem. Int. Ed. Engl.* 57 (2018) 14188–14192.
- [14] H. Zhang, Y. Kim, Y. Hu, J. Lee, A few atomic FeNbO₄ overlayers on hematite nanorods: microwave-induced high temperature phase for efficient photoelectrochemical water splitting, *ACS Catal.* 9 (2019) 1289–1297.
- [15] O. Buyukcakir, S.H. Je, D.S. Choi, S.N. Talapaneni, Y. Seo, Y. Jung, K. Polychronopoulou, A. Coskun, Porous cationic polymers: the impact of counteranions and charges on CO_2 capture and conversion, *Chem. Commun.* 52 (2016) 934–937.
- [16] H. Ou, X. Chen, L. Lin, Y. Fang, X. Wang, Biomimetic donor–acceptor motifs in conjugated polymers for promoting exciton splitting and charge separation, *Angew. Chem. Int. Ed. Engl.* 57 (2018) 8729–8733.
- [17] J. Jiang, F. Su, A. Trewin, C. Wood, H. Niu, J.T.A. Jones, Y.Z. Khimyak, A. I. Cooper, Synthetic control of the pore dimension and surface area in conjugated microporous polymer and copolymer networks, *J. Am. Chem. Soc.* 130 (2008) 7710–7720.
- [18] S.-Y. Ku, M.A. Brady, N.D. Treat, J.E. Cochran, M.J. Robb, E.J. Kramer, M. L. Chabiny, C.J. Hawker, A modular strategy for fully conjugated donor–acceptor bloc copolymers, *J. Am. Chem. Soc.* 134 (2012) 16040–16046.
- [19] S. Wang, X. Wang, Imidazolium ionic liquids, imidazolidene heterocyclic carbenes, and zeolitic imidazolate frameworks for CO_2 capture and photochemical reduction, *Angew. Chem. Int. Ed. Engl.* 55 (2016), 2308–20.
- [20] J. Lin, Z. Ding, Y. Hou, X. Wang, Direct observation of ion distributions near electrodes in ionic polymer actuators containing ionic liquids, *Sci. Rep.* 3 (2013) 973.
- [21] A. Wagner, C. Sahn, E. Reisner, Towards molecular understanding of local chemical environment effects in electro- and photocatalytic CO_2 reduction, *Nat. Catal.* 3 (2020) 775–786.
- [22] N. Huang, P. Wang, M.A. Addicoat, T. Heine, D. Jiang, Ionic covalent organic frameworks: design of a charged interface aligned on 1D channel walls and its unusual electrostatic functions, *Angew. Chem. Int. Ed.* 56 (2017) 4982–4986.
- [23] M.M. Cetin, Y. Beldjoudi, I. Roy, O. Anamimoghdam, J.F. Stoddart, Combining intra- and intermolecular charge transfer with polycationic cyclophanes to design 2D tessellations, *J. Am. Chem. Soc.* 141 (2019) 18727–18739.
- [24] Z. Mi, P. Wang, R. Wang, J. Unruangsri, J. Guo, Stable radical cation-containing covalent organic frameworks exhibiting remarkable structure-enhanced photothermal conversion, *J. Am. Chem. Soc.* 141 (2019) 14433–14442.
- [25] S. Li, L. Li, Y. Li, L. Dai, B. Wang, Fully conjugated donor–acceptor covalent organic frameworks for photocatalytic oxidative amine coupling and thioamide cyclization, *ACS Catal.* 10 (2020) 8717–8726.
- [26] W. Yang, J. Zhang, R. Si, L. Cao, D. Zhong, T. Lu, Fully conjugated donor–acceptor covalent organic frameworks for photocatalytic oxidative amine coupling and thioamide cyclization, *Inorg. Chem. Front.* 8 (2021) 1695–1701.
- [27] J. Li, D. Zhao, J. Liu, A. Liu, D. Ma, Covalent organic frameworks: a promising materials platform for photocatalytic CO_2 reductions, *Molecules* 25 (2020) 2425.
- [28] S. Wang, X. Hai, X. Ding, S. Jin, Y. Xiang, P. Wang, B. Jiang, F. Ichihara, M. Oshikiri, X. Meng, Y. Li, W. Matsuda, J. Ma, S. Seki, X. Wang, H. Huang, Y. Wada, H. Chen, J. Ye, Intermolecular cascaded π -conjugation channels for electron delivery powering CO_2 photoreduction, *Nat. Commun.* 11 (2020) 11149.
- [29] Z. Zhang, Y. Zhu, X. Chen, H. Zhang, J. Wang, A full-spectrum metal-free porphyrin supramolecular photocatalyst for dual functions of highly efficient hydrogen and oxygen evolution, *Adv. Mater.* 31 (2019), 1806626.

- [30] Z. Zhang, X. Chen, H. Zhang, W. Liu, W. Zhu, Y. Zhu, In situ grazing-incidence wide-angle scattering reveals mechanisms for phase distribution and disorientation in 2D halide perovskite films, *Adv. Mater.* 32 (2020), 2002812.
- [31] W. Zhou, L. Yang, F. Zhou, Q. Deng, X. Wang, D. Zhai, G. Ren, K. Han, W. Deng, L. Sun, Salen-based conjugated microporous polymers for efficient oxygen evolution reaction, *Chemistry* 26 (2020) 7720–7726.
- [32] Q. Lv, W. Si, J. He, L. Sun, C. Zhang, N. Wang, Z. Yang, X. Li, X. Wang, W. Deng, Y. Long, C. Huang, Y. Li, Selectively nitrogen-doped carbon materials as superior metal-free catalysts for oxygen reduction, *Nat. Commun.* 9 (2018) 3376.
- [33] Y. Xie, T. Wang, X. Liu, K. Zou, W. Deng, Capture and conversion of CO₂ at ambient conditions by a conjugated microporous polymer, *Nat. Commun.* 4 (2013) 1960.
- [34] S. Yang, X. Lin, W. Lewis, M. Suyetin, E. Bichoutskaia, J.E. Parker, C.C. Tang, D. R. Allan, P.J. Rizkallah, P. Hubberstey, N.R. Champness, K.M. Thomas, A.J. Blake, M. Schröder, A partially interpenetrated metal-organic framework for selective hysteretic sorption of carbon dioxide, *Nat. Mater.* 11 (2012) 710–716.
- [35] W. Zhong, R. Sa, L. Li, Y. He, L. Li, J. Bi, Z. Zhuang, Y. Yu, Z. Zou, A covalent organic framework bearing single Ni sites as a synergistic photocatalyst for selective photoreduction of CO₂ to CO, *J. Am. Chem. Soc.* 141 (2019) 7615–7621.
- [36] R. Chen, J.-L. Shi, Y. Ma, G. Lin, X. Lang, C. Wang, Designed synthesis of a 2D porphyrin-based sp² carbon-conjugated covalent organic framework for heterogeneous photocatalysis, *Angew. Chem. Int. Ed. Engl.* 58 (2019) 6430–6434.
- [37] X. Kang, B. Wang, K. Hu, L. Kai, M. Schröder, Quantitative electro-reduction of CO₂ to liquid fuel over electro-synthesized metal-organic frameworks, *J. Am. Chem. Soc.* 142 (2020) 17384–17392.
- [38] Y. Xie, Z. Fang, L. Li, H. Yang, T. Liu, Creating chemisorption sites for enhanced CO₂ photoreduction activity through alkylamine modification of MIL-101-Cr, *ACS Appl. Mater. Interfaces* 11 (2019) 27017–27023.
- [39] G. Cheng, B. Bonillo, R.S. Sprick, D.J. Adams, T. Hasell, A.I. Cooper, Conjugated polymers of intrinsic microporosity (C-PIMs), *Adv. Funct. Mater.* 24 (2014) 5219–5224.
- [40] W. Zhou, W. Deng, G. Ren, L. Sun, L. Yang, Y. Li, D. Zhai, Y. Zhou, W. Deng, Enhanced carbon dioxide conversion at ambient conditions via a pore enrichment effect, *Nat. Commun.* 11 (2020) 4481.
- [41] C. Huang, C. Chen, M. Zhang, L. Lin, X. Ye, S. Lin, M. Antonietti, X. Wang, Carbon-doped BN nanosheets for metal-free photoredox catalysis, *Nat. Commun.* 6 (2015) 7698.
- [42] M. Lu, Q. Li, J. Liu, F. Zhang, L. Zhang, J. Wang, Z. Kang, Y. Lan, Installing earth-abundant metal active centers to covalent organic frameworks for efficient heterogeneous photocatalytic CO₂ reduction, *Appl. Catal. B- Environ.* 254 (2019) 624–633.
- [43] M. Tan, Y. Xiao, W. Xi, X. Lin, B. Gao, Y. Chen, Y. Zheng, B. Lin, Cobalt-nanoparticle impregnated nitrogen-doped porous carbon derived from Schiff-base polymer as excellent bifunctional oxygen electrocatalysts for rechargeable zinc-air batteries, *J. Power Sources* 490 (2021), 229570.
- [44] Z. Wu, L. Chen, J. Liu, K. Parvez, H. Liang, J. Shu, H. Sachdev, B. Graf, X. Feng, K. Müllen, High-performance electrocatalysts for oxygen reduction derived from cobalt porphyrin-based conjugated mesoporous polymers, *Adv. Mater.* 26 (2014) 1450–1455.
- [45] C. Yang, W. Huang, L.C.D. Silva, K.A.I. Zhang, X. Wang, Functional conjugated polymers for CO₂ reduction using visible light, *Chemistry* 24 (2018) 17454–17458.
- [46] J. Qin, S. Wang, H. Ren, Y. Hou, X. Wang, Photocatalytic reduction of CO₂ by graphitic carbon nitride polymers derived from urea and barbituric acid, *Appl. Catal. B- Environ.* 279 (2015) 1–8.
- [47] J.H. Lee, S. Kattel, Z. Jiang, Z. Xie, S. Yao, B.M. Tackett, W. Xu, N.S. Marinkovic, J. G. Chen, Tuning the activity and selectivity of electroreduction of CO₂ to synthesis gas using bimetallic catalysts, *Nat. Commun.* 10 (2019) 3724.
- [48] M. Kathe, A. Empfield, P. Sandvik, C. Fryer, Y. Zhang, E. Blaira, L.-S. Fan, Utilization of CO₂ as a partial substitute for methane feedstock in chemical looping methane-steam redox processes for syngas production, *Energy Environ. Sci.* 10 (2017) 1345–1349.
- [49] G.A. Olah, Towards oil independence through renewable methanol chemistry, *Angew. Chem. Int. Ed.* 52 (2013) 104–107.
- [50] D. Yang, Q. Zhu, X. Sun, C. Chen, W. Guo, G. Yang, B. Han, Electrosynthesis of a defective indium selenide with 3D structure on a substrate for tunable CO₂ electroreduction to syngas, *Angew. Chem. Int. Ed.* 132 (2020) 2374–2379.
- [51] S. Kuld, M. Thorhauge, H. Falsig, C.F. Elkjær, S. Helveg, I. Chorkendorff, J. Sehested, Quantifying the promotion of Cu catalysts by ZnO for methanol synthesis, *Science* 352 (2016) 969–974.
- [52] P. Kumar, C. Joshi, N. Labhsetwar, R. Boukherroubc, S.L. Jain, A novel Ru/TiO₂ hybrid nanocomposite catalyzed photoreduction of CO₂ to methanol under visible light, *Nanoscale* 7 (2015) 15258–15267.
- [53] L. Hao, L. Kang, H. Huang, L. Ye, K. Han, S. Yang, H. Yu, Surface-halogenation-induced atomic-site activation and local charge separation for superb CO₂ photoreduction, *Adv. Mater.* 31 (2019), 1900546.
- [54] S. Zhang, G. Cheng, L. Guo, N. Wang, B. Tan, S. Jin, Strong-base-assisted synthesis of a crystalline covalent triazine framework with high hydrophilicity via benzylamine monomer for photocatalytic water splitting, *Angew. Chem. Int. Ed.* 59 (2020) 6007–6014.
- [55] K. Gelderman, L. Lee, S.W. Donne, Flat-band potential of a semiconductor: using the mott-schottky equation, *J. Chem. Educ.* 84 (2007) 685.
- [56] W. Luo, Z. Yang, Z. Li, J. Zhang, J. Liu, Z. Zhao, Z. Wang, S. Yan, T. Yu, Z. Zou, Solar hydrogen generation from seawater with a modified BiVO₄ photoanode, *Energy Environ. Sci.* 4 (2011) 4046–4051.